geosciences

MDPI

Article

Arsenic Mineral in Volcanic Tuff, a Source of Arsenic Anomaly in Groundwater: City of Chihuahua, Mexico

Minghua Ren [1,*], José Alfredo Rodríguez-Pineda [2] and Philip Goodell [3]

[1] Department of Geoscience, University of Nevada Las Vegas, Las Vegas, NV 89154, USA
[2] World Wildlife Fund (WWF-Mexico, Water Management Program), Colonia Guadalupe, Chihuahua 31410, Mexico; alrodriguez@wwfmex.org
[3] Department of Geological Sciences, University of Texas at El Paso, El Paso, TX 79968, USA; goodell@utep.edu
* Correspondence: minghua.ren@unlv.edu

Abstract: Arsenic is a naturally occurring trace element that causes many health effects when present in drinking water. Elevated arsenic concentrations in water are often attributed to nearby felsic volcanic sequences; however, the specific rock units to which the groundwater anomalies can be accredited are rarely identified. The groundwater from wells around the city of Chihuahua, Mexico, contains high arsenic content. Arsenic in groundwater increases toward the base rock containing Tertiary volcanic rocks. Through detailed scanning electron microscope (SEM) and electron microprobe (EMP) work, arsenic minerals are identified in the cavities of the Tertiary volcanic tuff from the northeast part of the Tabalaopa Basin, city of Chihuahua. Arsenic minerals, the As–Sr–Al phase (a possible arsenogoyazite–arsenoflorencite group mineral) crystallized in the vesicles of the tuff and the As–Y bearing phase included in biotite, prevail in the studied Tertiary volcanic outcrops. Based on the current study, the arsenic anomaly in the Tabalaopa–Aldama aquifer corresponds to these arsenic phases in the Tertiary volcanic rocks.

Keywords: arsenic; Tertiary magmatism; tuff; arsenogoyazite; arsenoflorencite; REE

check for updates

Citation: Ren, M.; Rodríguez-Pineda, J.A.; Goodell, P. Arsenic Mineral in Volcanic Tuff, a Source of Arsenic Anomaly in Groundwater: City of Chihuahua, Mexico. *Geosciences* **2022**, *12*, 69. https://doi.org/10.3390/geosciences12020069

Academic Editors: Nicolò Colombani and Jesus Martinez-Frias

Received: 11 December 2021
Accepted: 26 January 2022
Published: 1 February 2022

Publisher's Note: MDPI stays neutral with regard to jurisdictional claims in published maps and institutional affiliations.

Copyright: © 2022 by the authors. Licensee MDPI, Basel, Switzerland. This article is an open access article distributed under the terms and conditions of the Creative Commons Attribution (CC BY) license (https://creativecommons.org/licenses/by/4.0/).

1. Introduction

High arsenic concentrations in drinking water have been linked to diverse types of diseases [1]. Arsenic has been associated with cancer since 1879 when miners in Saxony presented high lung cancer rates [2]. Epidemiological studies in Argentina, Taiwan, Chile, Japan, Mexico, and Bangladesh have associated high arsenic in drinking water with skin, kidney, lung, and bladder cancers [3]. Contamination of drinking water sources with naturally occurring arsenic is a widespread environmental concern that affects the health of millions of people worldwide [4]. Various studies have suggested that the dissolution of arsenic-bearing minerals can be the primary source of arsenic in groundwater [5,6].

The city of Chihuahua, in the semiarid area of northern Mexico, relies on the groundwater system as the main source of potable water. The annual precipitation in the city region is 332 mm and the annual potential evaporation ranges between 2300 and 2600 mm [7]. Rapid urban development during the last 50 years has resulted in a large decrease in the groundwater levels of the aquifers in the region [8]. This makes the groundwater from the surrounding area to be the major supplier for Chihuahua urban areas. The Chihuahua–Sacramento, El Sauz–Encinillas, and Tabalaopa–Aldama aquifers are the major groundwater resources for the city of Chihuahua. The main aquifers are hosted in the unconsolidated Quaternary alluvial sediments, Tertiary volcanic rocks and volcanic sediments, and Cretaceous sediments. Arsenic content in the wells is more than 20 ppb in Tabalaopa–Aldama aquifer [7] and more than 10 ppb in the Chihuahua–Sacramento [8]. The arsenic concentration in groundwater is elevated toward the northeast (Figure 1). The groundwater from the aforementioned wells shows that the arsenic contents are higher

in the Tabalaopa–Aldama aquifer toward the northeast (Sierra del Cuervo) [7] and the Chihuahua–Sacramento aquifer toward the northwest (Sierra Sacramento) [8].

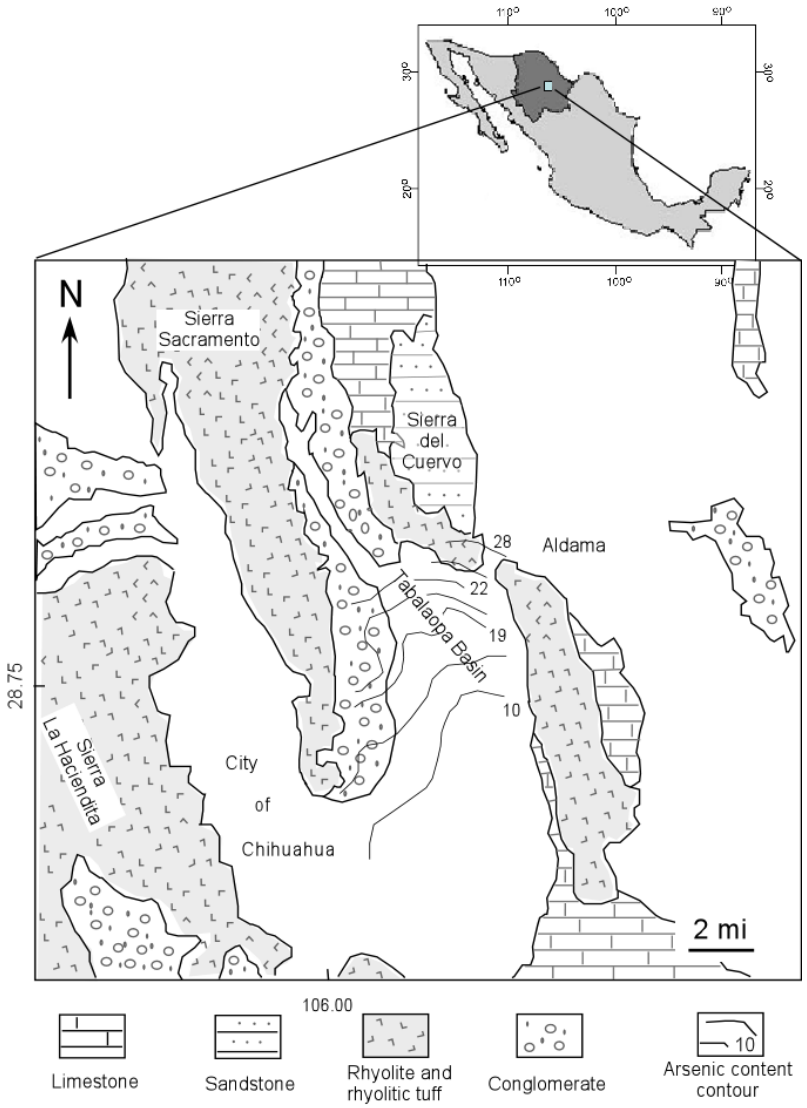


Figure 1. Simplified geological map of the studied area (modified from Carta Geologica de la Republica Mexicana [9]). Arsenic contour is based on the arsenic content in the wells (not indicated in this map, data, from Rodríguez-Pineda (2000) [7], plot by software "Surfer" with Kriging interpolation method).

Cenozoic volcanic tuff at the Tabalaopa Basin has been studied in this work to track the source of arsenic in groundwater near the city of Chihuahua, Mexico. Arsenic minerals are identified in the tuff through petrographic and mineral chemistry study from this work. The major arsenic-containing mineral is the As–Sr–Al arsenate, which contains high contents of REE. Detailed SEM and EPM data of this arsenate, minerals in the tuff, and major and trace elements of the tuff are presented in this paper.

2. Regional Geology

The studied area is in the low hill region of Sierra del Cuervo, a southern extension of the Sierra del Cuervo-Peña Blanca range at the northeast of Tabalaopa Basin. The contour of high groundwater arsenic points to the volcanic rocks of the Sierra del Cuervo range (Figure 1). Tabalaopa Basin, located at the joint place between Sierra Sacramento block and Sierra del Cuervo block (Figure 1), is a block-faulted mountain range that lies within the transition zone between the Mexican part of the Basin and Range province to the east and

the Sierra Madre Occidental to the west [10,11]. It has long been recognized that Sierra del Cuervo contains one of the most lithological different Paleozoic outcrops in Chihuahua [11]. Late Precambrian to Quaternary rocks exposed in the mountain range and the strata sequences in the region are as follows: Tertiary volcanic rocks cover Cretaceous carbonates, the Mesozoic carbonates overlie the late Paleozoic intensely folded and faulted, and weakly metamorphosed sandstones and shales; Precambrian crystalline rocks are included in the late Paleozoic Pennsylvanian to Lower Permian sediments. These late Paleozoic rocks and the contained Precambrian units have lithological and temporal similarities to the Ouachita facies of west Texas [10,12]. The distribution of carbonates indicates that the Sierra del Cuervo-Sierra Peña Blanca block was located along the boundary between the Chihuahua trough to the east and the Aldama platform to the west during the Cretaceous [13]. Normal faults developed in the late Cenozoic affected the sedimentary sequence of Mesozoic strata and the structures in the Sierra del Cuervo range. The late Cenozoic faults may correspond to the development of the Rio Grande Rift [14].

Throughout the region from Cuchillo Parado to Aldama, Tertiary volcanic and hypabyssal intrusive rocks are widely exposed. The mid-Tertiary rhyolitic eruptions blanket the region. The volcanic rocks mainly contain sequences of pyroclastic tuffs with rhyolitic composition. The tuffs reach a thickness of up to 1000 m in the Sierra del Cuervo range and are highly permeable due to high matrix porosity [9]. The silicic ignimbrites and rhyolite flows unconformably overlie the low angle dipping shelf and basinal faces of the thick sequence of Cretaceous carbonates and late Paleozoic weakly metamorphosed sandstone and shales [15]. Tertiary volcanic activities in the region might be part of the ignimbrite flare-up and deformation of the Sierra Madre Occidental, Mexico. Oligocene episodes of ignimbrite flare-up were coeval over a large area from the United States–Mexico border to the south of the Trans-Mexican Volcanic Belt.

The Tertiary silicic flare-up has been related to the rolled back and foundered in the mantle of the Farallon slab beneath the North America plate, and the melting of the crust played an important role in generating this massive silicic volcanism [16,17]. The volcanic activities started from east to west in the northern Sierra Madre Occidental (SMO) [18]. The easternmost extent of the Sierra Madre Occidental volcanic field reaches the Sierra del Cuervo range [19]. Tertiary volcanic and hypabyssal intrusive rocks are common throughout the Sierra del Cuervo range. Calc-alkalic rhyolite suites and peralkaline rhyolitic tuffaceous units developed in the mid-Tertiary volcanic activities [20,21]. Calc-alkalic suites contain ferromagnesian minerals and reflect the high oxygen fugacity condition of the calc-alkalic magmas [22,23]. Peralkaline rhyolitic ignimbrites distinctly different from the regional calcalkaline rocks occur near the city of Chihuahua and are extensively distributed in the area to the north of the city of Chihuahua [11,22]. The bulk composition of these rocks nearly reaches the peralkaline borderline [22]. Rhyolites of this suite are distinguishable from those of the calc-alkalic suite by the presence of Fe-rich clinopyroxene ± fayalite in fresh samples. The alkali rhyolites are dated from 27.8 to 31.5 Ma [22,24] in the north of the city of Chihuahua and from 30 to 38 Ma south of Sierra Sacramento and east of Sierra La Haciendita [11].

3. Methods

Twelve pinkish-gray volcanic tuffs were collected from the Sierra del Cuervo region. Nine rock chips have been mounted in epoxy to shape as 1″ rounds and polished for scanning electron microscope (SEM) and electron probe microanalysis (EPMA) study. Instruments used in this study included Cameca SX50 microprobe at University of Texas at El Paso, JEOL JXA8900 microprobe, JSM5600 SEM, and JSM6700F field emission SEM at University of Nevada Las Vegas. Secondary and backscattered electron images (SEI and BSEI) and energy dispersive spectrometry (EDS) were collected from JSM5600 and JSM6700F in UNLV. Mineral chemistry elemental X-ray maps were obtained by electron probe micro-analyzer (EPMA) from both UTEP and UNLV. Whole section elemental X-ray maps (Fe-S-As-Al) have been obtained from samples to detect arsenic phase distribution and other minerals in the samples. The X-ray map condition was 20 kV accelerating voltage

and 100 nA beam current with a focused beam. The major arsenic signals were in the vesicles of the rocks. The EDS peaks and EPMA wavelength peak scan showed that arsenic mineral has a chemistry of As–Al–Sr-(P)-REE components.

The mineral chemical analyses were performed under the condition of 15 kV accelerating voltage, 10 nA beam current, focused beam to 10 µm beam size, and 30 seconds peak counting time for analyzed elements. Calibration standards include Smithsonian plagioclase for SiO_2, and CaO; corundum for Al_2O_3; chromite for Cr_2O_3; ilmenite for TiO_2 and FeO; olivine for MaO; albite for Na_2O; microcline for K_2O, and apatite for P_2O_5. Fluorite, AgCl, and pyrite have been used as F, Cl, and S standards. Synthetic REE phosphates, zircon, and barite were used as REE, Y, Zr, and Ba standards. The full data are reported in Supplementary Materials SI.

Whole-rock major and trace element analyses from five rocks were collected with iCAPTM Qc ICP-MS from Thermo ScientificTM, with a CetacTM ASX520 autosampler at UNLV. Around 500 mg of the splits of crushed rocks were prepared by milling to <200 µm in an agate mill. Millipore ultrapure water (resistivity = 18 MΩ), double-distilled acids using a subboiling PFA distiller and Baseline/Optima grade acids were used for the sample preparation. The rock powder (~50 mg) of the sample was dissolved in 3 mL of a 1:1 mix of HF:HNO_3 in acid-cleaned Savillex beakers. Samples were then dried down and rehydrated with 1 mL of 50% HNO_3 (by mass) and dried back down three separate times. Then, 6 mL of 50% HNO_3 was added to each sample and no undissolved residue was observed. An aliquot (2 mL) of each sample solution was diluted with 2% HNO_3 in acid-cleaned 125 mL plastic bottles to a dilution factor of ~5000 for ICP-MS analysis.

4. Results

4.1. Petrographic Characteristics

The Tertiary volcanic tuff samples have been collected to track the potential arsenic source. The collected volcanic samples are reddish welded ash-flow tuff and rhyolite. The outcrop of volcanic field is presented in Supplementary Materials SII. The fresh exposures of the rock are grayish color, porphyritic with mainly alkali feldspar (15%), quartz (10%), small biotite (5%), and small black specks of specular hematite/limonite. Small vesicles (0.2–0.5 × 1–2 mm) are aligned with flow bends. Within the vesicles, there are micron-size honey-colored crystals. The studied samples are described below.

Samples e84, e111, and e116 are densely welded tuff with a pinkish color. Pumice fragments and cavities are flattened and curved (Figure 2b). Feldspar and biotite phenocrysts are distributed parallel to the flow foliation. Small anhedral oxides exist in the matrix. There are arsenic minerals in the matrix and vesicles.

Samples e65, e69, and e115 are brown to pinkish-grey partially welded ash-flow tuff. The rock contains anhedral quartz and K-feldspar phenocrysts and flattened pumices. Lithics are up to 0.3 cm and take 15% of rock volume (Figure 2a). Flattened pumices distribute near parallel in the rock. Vesicles are aligned with the fiamme lineation in a layer orientation. Arsenic minerals are abundant and mainly clustered in the vesicles. Backscatter electron images show that euhedral crystals with around 10 microns are the major arsenic phases (Figure 3). Biotite phenocryst can contain As–Y mineral inclusion (Figure 4a). Micron size crystals of euhedral feldspar, ilmenite, quartz, and euhedral zircon are also crystallized in the vesicles (Figure 4b,c).

Samples e93 and sa3 are non-welded tuff with red to reddish-brown color. The pumices in these rocks are irregular in shape and not orientated. Large numbers of gas holes are included in pumice (Figure 2c). Sa3 has a significantly different petrographic feature than the e93. Sa3 has only a few pumices but many mineral fragments. The rock has smaller-sized vesicles, and arsenic mineral is barely found in this rock.

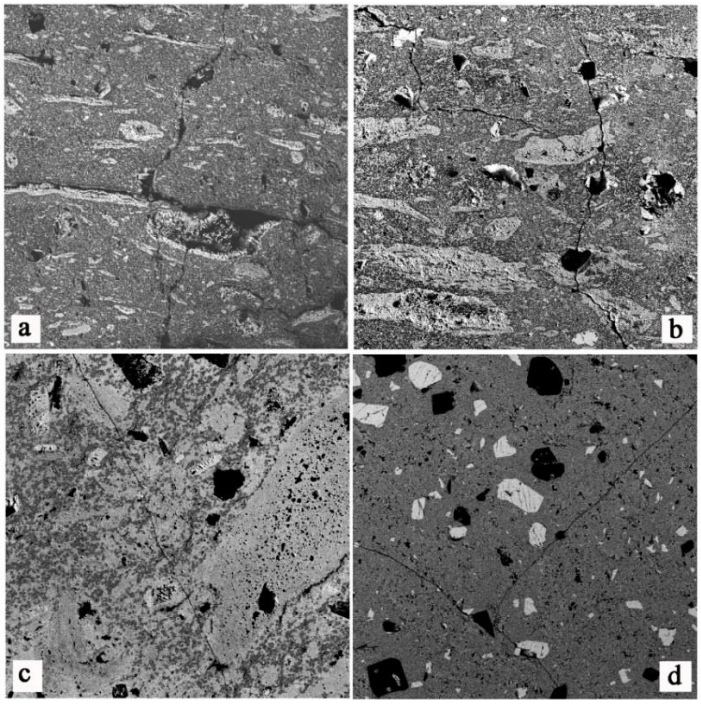


Figure 2. Whole-section Al X-ray maps show the petrographic characters of Tertiary volcanic tuff (brighter patches in the image indicate a higher amount of aluminum content, vesicles show as dark in the image, except in (**d**), where quartz shows as dark). Each image covers 2 cm^2 area. (**a**) Densely welded tuff, all pumices are flattened. (**b**) Partially welded tuff, pumices form lens shape. (**c**) Non-welded tuff, gas vesicles are preserved in the pumice. (**d**) Rhyolite, sanidine and quartz phenocrysts are randomly distributed in the matrix.

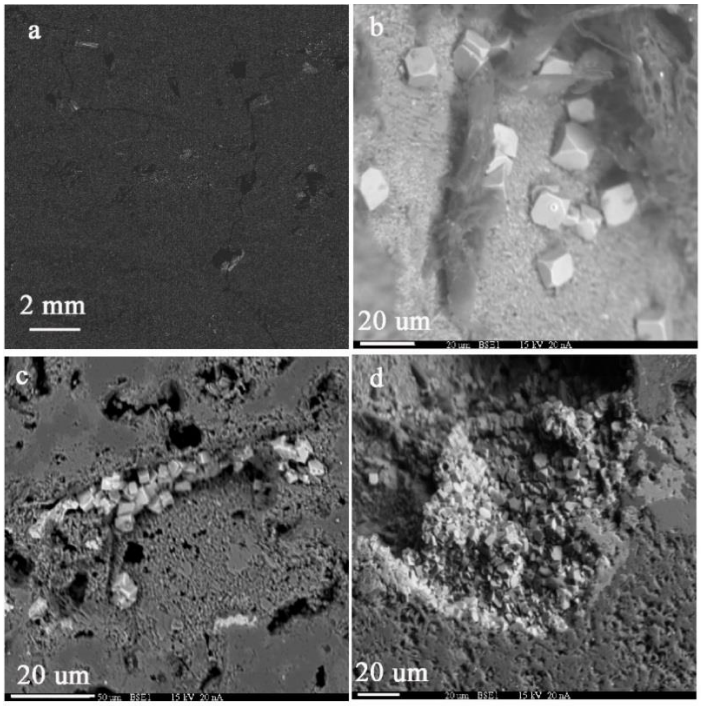


Figure 3. Arsenic minerals in the rock. (**a**) Arsenic X-ray map shows the distribution of arsenic minerals (bright patches in the rock, mainly in the vesicle areas). (**b**–**d**) Arsenogoyazite crystals gather in the cavities.

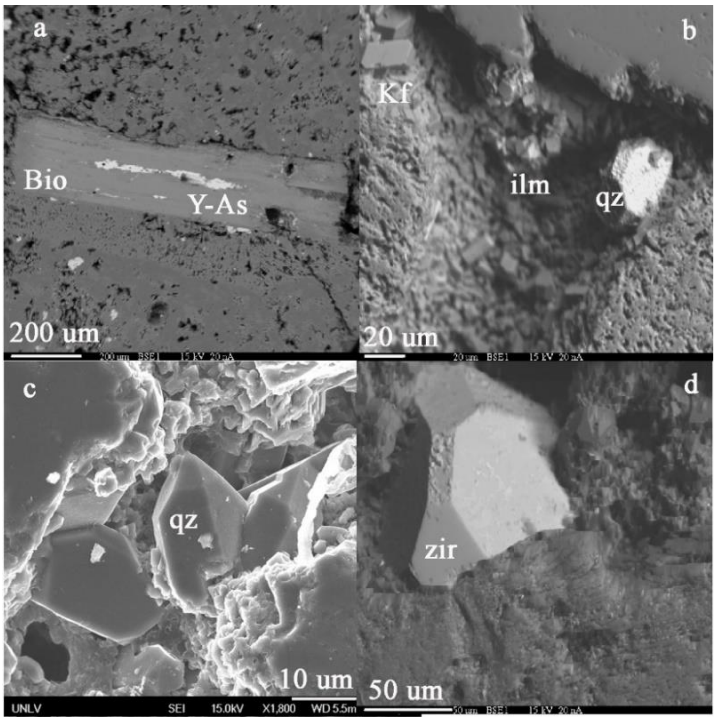


Figure 4. Different types of arsenic phases and their relations with other minerals. (**a**) As–Y phase (Y–As) included in biotite (Bio). (**b**) Euhedral sanidine (Kf), ilmenite (ilm), and quartz (qz) coexist with arsenogoyazite-like crystals in the vesicle. (**c**) Euhedral quartz and sanidine in the vesicle. (**d**) Euhedral zircon in the vesicle.

Sample e112 is rhyolite. It contains around 20% of subhedral quartz and feldspar (up to several mm in size) (Figure 2d). Small honey-colored arsenic minerals exist in vesicles.

4.2. Volcanic Shard and Mineral Chemistry

Microprobe analyses for volcanic shard and minerals are listed in Tables 1–4 and Supplementary Materials SI.

4.2.1. Volcanic Shard

Representative microprobe analyses of shards in pumices are listed in Table 1. Other than the sample sa3, the shard compositions of all tuffs fall in the rhyolite field in the TAS diagram (Figure 5). SiO_2 ranges from 68 to 89 wt.%, Al_2O_3 from 15 to wt.%, Na_2O from 0.5 to 2 wt.%, and K_2O from 4 to 15 wt.%. FeO and CaO are generally less than 0.05 wt.%. Ba and Sr are detectable and can reach up to 0.1 wt.% oxides. The Aluminum Saturation Index ((ASI − Al/(Ca − 1.67P + Na + K)) ranges from 0.92 to 1.03, and the Agpaitic Index ((AI − (Na + K)/Al) is generally less than 1 with a few reaches to 1.01–1.03. The rock is potassium-rich and has metaluminous to weak peralkaline characteristics. The high SiO_2 content in some shard analyses may indicate a silicification process of the tuff, while the volcanic tuff is compacted in the subsolidus stage.

Table 1. Representative electron microprobe analyses of shard in the Tertiary volcanic tuff.

Sample	e65	e69	e84	e93	e112	e115	e116	sa3
SiO_2	82.38	76.74	70.47	76.18	78.20	77.75	72.57	64.66
TiO_2	bdl	0.10	0.07	0.15	0.15	bdl	0.02	0.19
Al_2O_3	8.61	10.90	15.75	12.64	10.97	10.95	14.21	18.77
FeO	0.14	0.28	0.35	0.38	0.53	0.15	0.33	0.83
MnO	bdl	bdl	bdl	bdl	0.06	bdl	0.02	0.03
MgO	0.04	0.14	0.04	bdl	bdl	0.01	0.03	0.27
CaO	0.10	0.55	0.23	0.09	0.03	0.20	0.28	0.75
Na_2O	0.73	1.37	1.75	1.20	1.71	1.24	1.45	3.90
K_2O	6.35	8.05	11.01	9.47	7.68	8.14	9.82	8.14
P_2O_5	0.01	0.03	0.02	bdl	bdl	bdl	0.04	0.10
F	bdl	0.09	0.14	bdl	bdl	0.03	bdl	0.03
Cl	0.02	0.02	0.02	0.01		0.02		bdl
SO_3	0.04	1.01	0.04	0.03		0.07		0.01
BaO	bdl	0.04	0.01	0.03	0.02	bdl	0.04	0.08
SrO		0.09	bdl	bdl	bdl	0.03	bdl	0.06
Total	98.63	99.35	99.84	100.23	99.36	98.57	98.81	97.92
TA	7.09	9.41	12.76	10.67	9.39	9.38	11.27	12.03
ASI	1.05	0.92	1.04	1.02	0.98	0.98	1.06	1.15
AI	0.94	1.01	0.94	0.97	1.01	0.99	0.92	0.81

Blank cell has no data. TA = K_2O + Na_2O. ASI—aluminum saturation index, AI—agpaitic index, bdl—below detection limit.

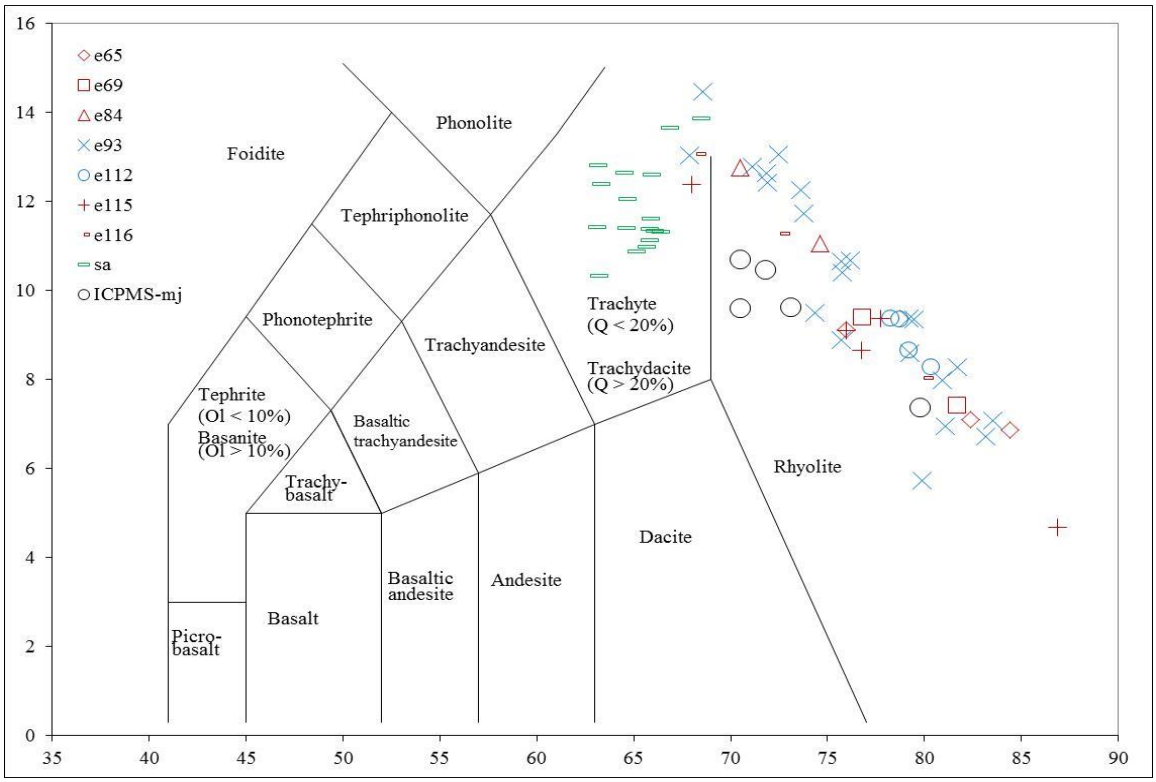


Figure 5. SiO_2 vs. total alkali (TAS) plot shows the shard chemistry. E- series samples are mainly in the rhyolite region with relatively high total alkali, and the SiO_2 increasing pattern might be caused by the silicification of the tuff in the diagenesis. The sample sa3 is a different volcanic unit. The ICP-MS whole-rock major data show as black circles.

Table 2. Representative feldspar analyses.

	e65		**e69**			**e84**			**e93**	**e111**
	ano	matrix	ano	sa	matrix	ano	sa	matrix	sa	sa
SiO_2	64.91	65.23	63.67	65.79	64.90	61.97	64.46	66.62	63.15	63.85
TiO_2	0.14	0.02	0.03	bdl	0.06	0.03	bdl	0.06	0.01	bdl
Al_2O_3	20.22	18.98	21.06	18.55	20.14	19.78	18.24	18.56	18.84	18.79
FeO	0.23	0.12	0.28	0.24	0.31	0.26	0.28	0.09	0.20	0.20
MnO	bdl	0.03	bdl	bdl	bdl	bdl	0.06	bdl	0.01	bdl
MgO	0.01	bdl	0.02	0.02	0.01	0.01	0.02	0.03	0.03	bdl
CaO	0.65	0.15	0.92	0.21	0.76	0.93	0.19	0.33	0.30	0.23
Na_2O	5.30	1.50	4.86	1.86	5.01	4.95	1.12	4.86	1.20	1.17
K_2O	8.68	13.80	8.33	13.22	8.87	7.97	14.94	9.31	14.81	14.99
P_2O_5	bdl	0.01	bdl	0.55	bdl	bdl	bdl	0.01	0.01	0.12
BaO	0.26	bdl	2.48	0.34	0.76	2.72	0.08	0.29	0.03	0.09
SrO	0.06	0.08	0.08	bdl	0.10	0.13	bdl	bdl	bdl	bdl
Total	100.46	99.95	101.75	101.15	101.00	98.77	99.48	100.26	98.67	99.70
An wt%	3.23	0.78	4.79	1.10	3.82	4.93	0.94	1.65	1.50	1.16
Ab wt%	45.16	13.38	43.33	16.56	43.01	44.74	9.57	42.06	10.20	9.92
Or wt%	51.62	85.85	51.88	82.35	53.17	50.33	89.49	56.29	88.29	88.92

	e111	**e112**	**e115**			**e116**		**sa3**	
	matrix	ano	ano	sa	matrix	ano	sa	ano	pl
SiO_2	65.52	66.78	62.31	65.31	63.94	63.42	65.27	66.51	59.26
TiO_2	0.07	0.05	bdl	0.13	bdl	0.13	0.22	0.12	0.00
Al_2O_3	19.65	19.19	20.79	17.87	18.88	20.92	18.63	19.82	25.15
FeO	0.09	0.24	0.23	0.14	0.16	0.20	0.13		
MnO	bdl	bdl	0.01	0.01	0.04	0.03	bdl	0.24	0.27
MgO	0.01	0.01	bdl	0.02	bdl	0.01	bdl	0.02	0.05
CaO	0.25	0.09	1.04	0.12	0.24	0.96	0.13	bdl	bdl
Na_2O	4.15	5.58	4.72	1.40	1.16	5.21	1.48	0.51	6.70
K_2O	10.61	8.86	8.04	14.10	14.58	7.59	14.56	6.92	6.93
P_2O_5	0.05	bdl	bdl	0.01	0.20	bdl	0.01	6.43	0.93
BaO	0.48	0.04	2.33	0.00	0.08	2.08	0.02	0.03	0.02
SrO	0.11	bdl	0.17	0.01	0.11	bdl	bdl	bdl	bdl
Total	101.02	100.84	99.83	99.28	99.46	100.59	100.45	100.62	99.60
An wt%	1.26	0.44	5.59	0.61	1.22	5.08	0.65	2.56	34.15
Ab wt%	35.47	47.19	43.11	12.37	10.11	47.06	12.59	59.07	60.24
Or wt%	63.27	52.37	51.30	87.02	88.67	47.86	86.76	38.37	5.61

ano—anorthoclase, matrix—feldspar in matrix, sa—sanidine, An—anorthite, Ab-albite, Or—orthoclase, bdl—below detection limit.

The sample sa3 is different from the other tuffaceous samples in its petrographic and chemical features. It contains a higher amount of small phenocryst fragments. The chemistry of the shard has lower SiO_2 (64–66%) and higher Na_2O (3–7%). This rock should generate from a different eruption. The shard chemistry and mineral assemblage of this rock indicate that the rock should belong to the calcalkaline volcanic system.

4.2.2. Feldspar

Representative alkali feldspar compositions are listed in Table 2. The alkali feldspars in the sample are anorthoclase and sanidine. The phenocrysts show three chemical groups (Figure 6), one group is anorthoclase (Or 45–55) with high BaO (An 2–5, Ab 40–50, and BaO 2–3.5 wt.%), one group is anorthoclase (Or 45–60) with a notable amount of BaO (An 0.5–2, Ab 35–50, and BaO 0.1–1 wt.%), and one group is sanidine (Or 70–90) with low BaO (An 0.5–2, Ab 10–30, and BaO < 0.1 wt.%). Feldspar micron crystals in the matrix have similar chemistry as the anorthoclase (Or 45–60), with a notable amount of BaO feldspar group.

Table 3. Representative biotite and greenalite analyses.

	e69	e111	e116	e93		sa3
	biotite	biotite	biotite	Greenalite		amphibole
SiO_2	35.71	30.42	30.69	42.92	36.80	50.58
TiO_2	7.09	4.61	5.84	0.06	0.11	0.48
Al_2O_3	15.53	14.34	13.34	0.14	0.14	3.09
Cr_2O_3				0.03	bdl	
FeO	14.24	20.15	18.31	51.18	57.36	6.68
MnO	0.92	1.41	1.27	0.15	0.24	0.15
MgO	12.30	13.16	13.44	0.02	0.01	15.76
CaO	0.05	1.86	0.28	0.07	0.05	20.54
Na_2O	0.77	1.00	0.63	0.11	0.11	0.38
K_2O	7.88	6.04	6.63	0.07	0.05	bdl
P_2O_5	0.03	0.15	0.03	bdl	bdl	0.01
F	2.79	2.80	2.99	bdl	bdl	0.04
Cl	0.05	0.11		0.01	0.01	bdl
SO_3	0.12	2.10		0.02	0.05	0.05
BaO	2.45	0.30	2.16	bdl	bdl	0.04
SrO	0.03	bdl	bdl			bdl
Total	98.75	97.21	94.33	94.87	95.46	97.75

Blank cell has no data. bdl—below detection limit.

Table 4. Representative arsenic phase analyses.

Sample	e65	e65	e69	e69	e84	e84	e93	e93	e69Y
SiO_2	bdl	bdl	bdl	bdl	bdl	bdl	bdl	bdl	bdl
TiO_2	0.515	bdl	0.105	0.017	0.06	bdl	bdl	0.19	0.55
Al_2O_3	32.71	35.68	32.20	32.14	31.13	35.88	35.83	31.59	0.20
Cr_2O_3	0.03	bdl	bdl	bdl	bdl	bdl	bdl	bdl	bdl
FeO	0.87	0.50	0.72	0.88	0.42	0.38	1.50	3.73	1.13
MnO	0.30	0.19	0.11	0.06	0.05	0.12	0.20	0.08	bdl
MgO	bdl	bdl	bdl	bdl	bdl	bdl	bdl	bdl	bdl
CaO	1.71	1.65	1.19	1.22	0.38	0.47	0.98	0.60	2.41
Na_2O	bdl	0.05	0.09	0.05	0.02	bdl	0.03	0.01	bdl
K_2O	1.13	0.05	0.09	0.44	0.41	0.22	0.09	0.08	0.04
P_2O_5	5.64	3.52	15.28	14.01	1.86	1.51	1.81	1.52	3.11
F	0.465	bdl	2.03	1.811	bdl	bdl	bdl	bdl	0.07
Cl	bdl	0.01	0.14	0.11	0.02	0.01	0.03	0.04	0.05
SO_3	0.18	0.15	0.06	0.08	0.08	0.16	0.09	0.08	bdl
As_2O_5	18.79	22.40	9.23	13.33	27.91	30.91	32.76	28.32	30.82
SrO	11.15	12.34	4.63	5.93	7.94	10.80	11.96	10.27	bdl
BaO	0.977		10.443	9.152	bdl				bdl
La_2O_3	2.72	6.58	2.02	1.68	3.95	3.89	2.74	1.97	0.66
Ce_2O_3	2.11	0.99	3.23	3.68	8.38	7.43	3.81	3.26	8.51
Pr_2O_3	0.72	0.72	0.45	0.41	0.69	0.64	0.76	0.28	1.26
Nd_2O_3	1.18	1.26	1.24	0.92	1.64	1.42	1.99	1.62	7.64
Y_2O_3	0.041	0.046	0.017	bdl	0.001	0.04	0.02	0.009	20.05
ZrO_2	0.368	0.014	2.915	2.921	bdl	bdl	bdl	bdl	1.71
Total	81.408	86.132	85.298	88.051	84.933	93.87	94.58	83.621	78.14

Blank cell has no data. bdl—below detection limit.

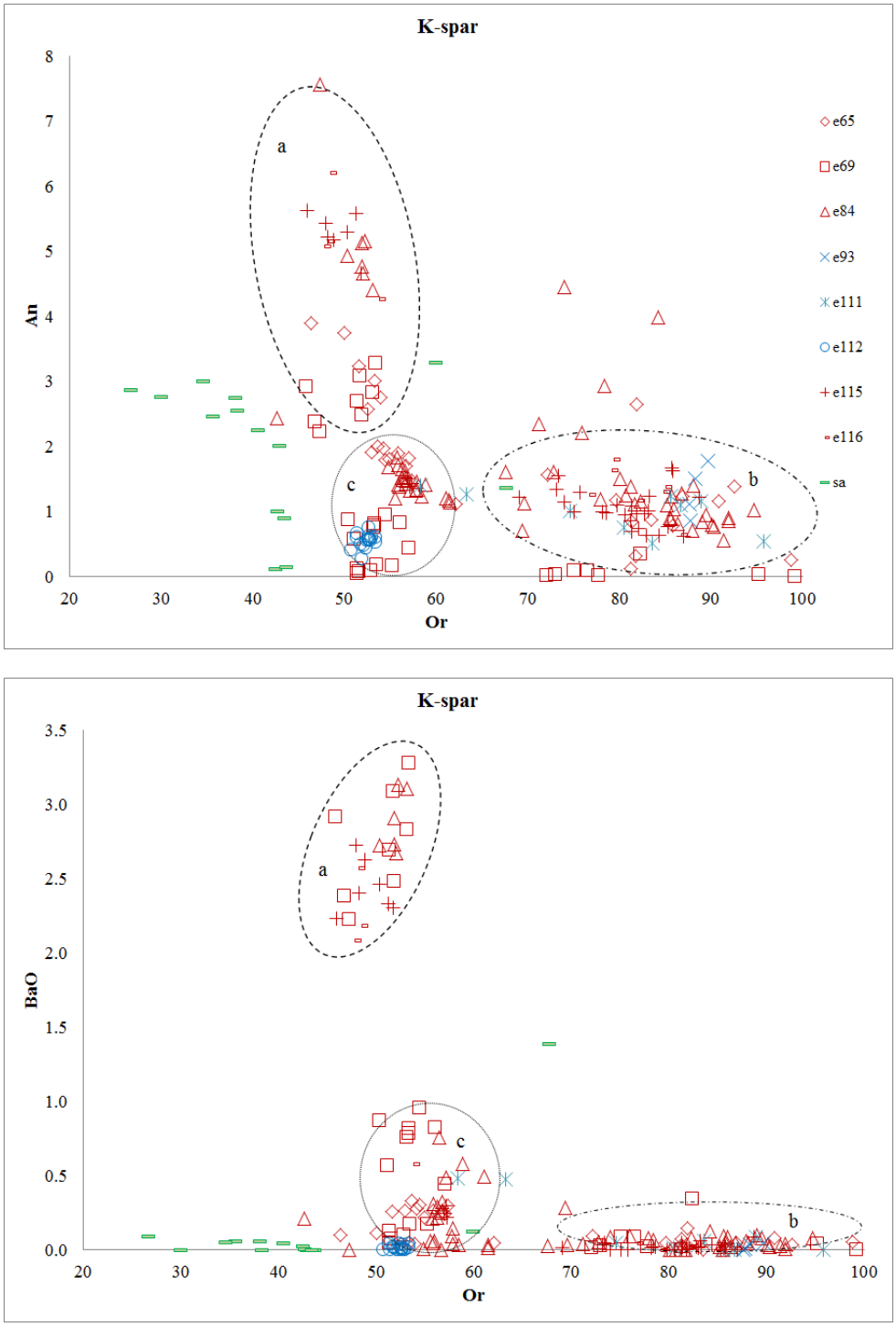


Figure 6. Feldspar chemical plots show the changes in mineral chemistry. There are different types of phenocrysts, (a) high BaO and high An group with Or around 50, (b) high K_2O and low BaO group with Or larger than 70, and (c) a group with 0.5 wt.% BaO and An ranging from 1–2. The sanidines in the matrix fall in the region of the medium amount BaO (0.3–1 wt.%) with Or around 50–60. The sample sa3 has low Or and low BaO. The different types of phenocrysts indicate that they may come from different sources.

Feldspar in sample sa3 has a different composition, the anorthoclase phenocrysts have low BaO (An 0.5–3, Ab 55–75, Or 25–45, and BaO < 0.5 wt.%), while the feldspars in the

matrix of sample sa3 are similar to the anorthoclase (Or 45–60) group in the tuffaceous rocks with a notable amount of BaO. Plagioclase (An 34) coexists with anorthoclase.

4.2.3. Biotite

Representative biotite compositions are listed in Table 3. Biotite phenocrysts are found in e69, e111, and e116. Biotites from samples e69 and e116 are BaO-rich with 2–3 wt.%. TiO_2 content in biotite ranges from 5–8 wt.%, MgO/(MgO + FeO) ranges mainly around 0.45 (within 0.35–0.7), MnO 0.3–1.5 wt.%, Na_2O 0.6–0.95 wt.%, K_2O 0.5–8.5 wt.%, F 1- 4.5 wt.%, and BaO 0.3–2.8 wt.%. BaO and TiO_2 show a positive correlation (Figure 7).

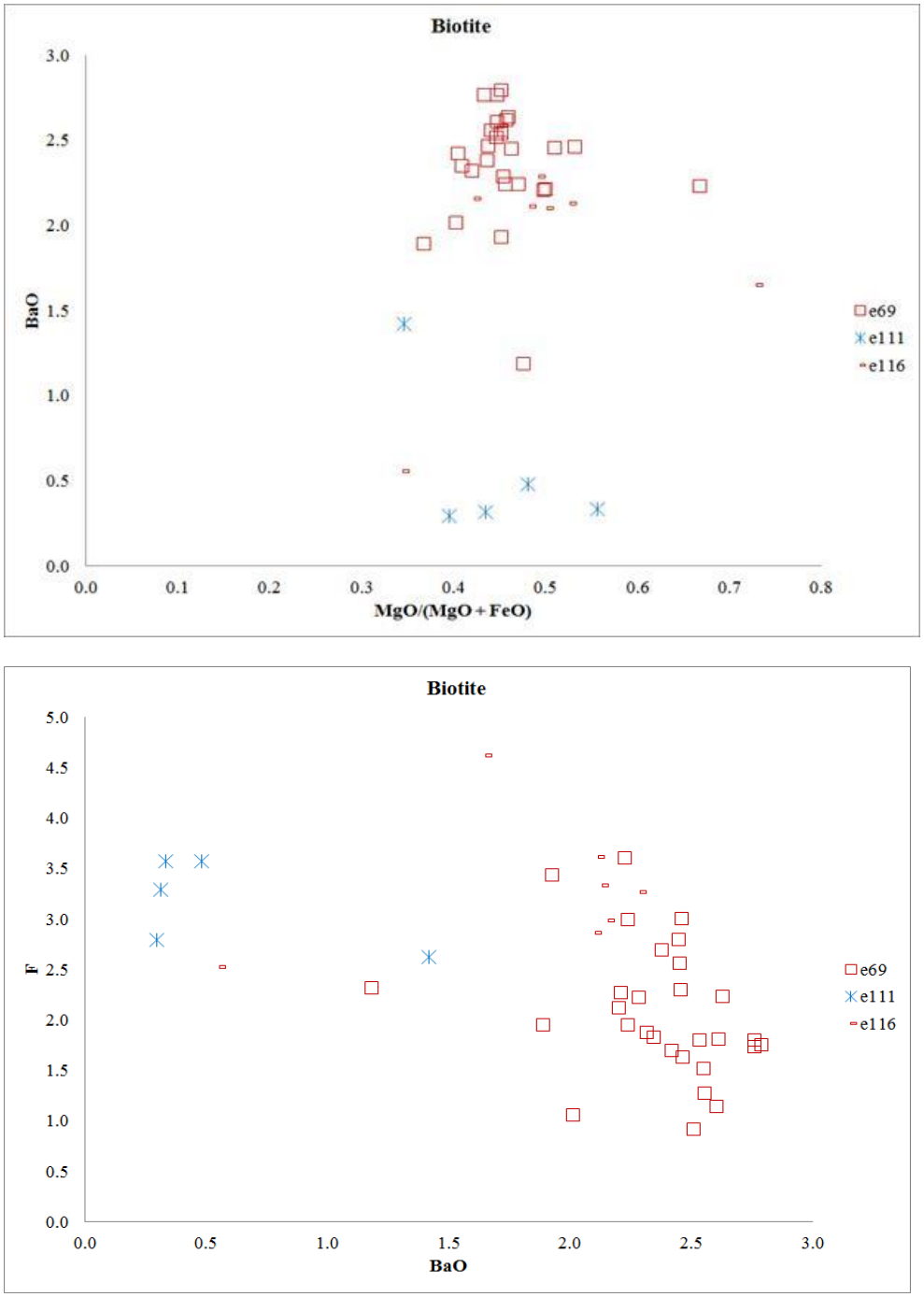


Figure 7. Biotite chemical plots show the changes in mineral chemistry. Biotite contains high BaO and F as well as high TiO_2 (Table 3).

4.2.4. Fe Oxides

There are both magnetite and ilmenite in the tuffs. Most magnetite and ilmenite are small anhedral grains in the matrix. The most common magnetite composition is in the range of TiO_2 2–4 wt.% and FeO 80–84 wt.%, ilmenite is TiO_2 in the range of 30–49 wt.% and FeO 40–55 wt.%. Some magnetite can have around 20 wt.% TiO_2, and some ilmenite can contain 60–65 wt.% TiO_2. Fe-oxide chemistry shows large variation.

4.2.5. Other Major Minerals

Alkali feldspar, biotite, magnetite, ilmenite, and quartz are the major phenocrysts in the rocks. A few other minerals are also found in the rocks. In e93, a hydrated Fe-Si mineral phase has FeO (51–58 wt.%), SiO_2 (36–43 wt.%) (Table 3 and Supplementary Materials SI) (Figure 8a), which might be altered from biotite. This mineral has a rounded shape, shows alteration on the rim, and contains magnetite grains. Based on the mineral chemistry, the Si-Fe hydrated phase might be greenalite, an iron-type serpentine. Plagioclase (An 27–34, Ab 60–67, Or 5–6) and amphibole (MgO/(MgO + FeO) 0.7) (Table 3) are found in sample sa3.

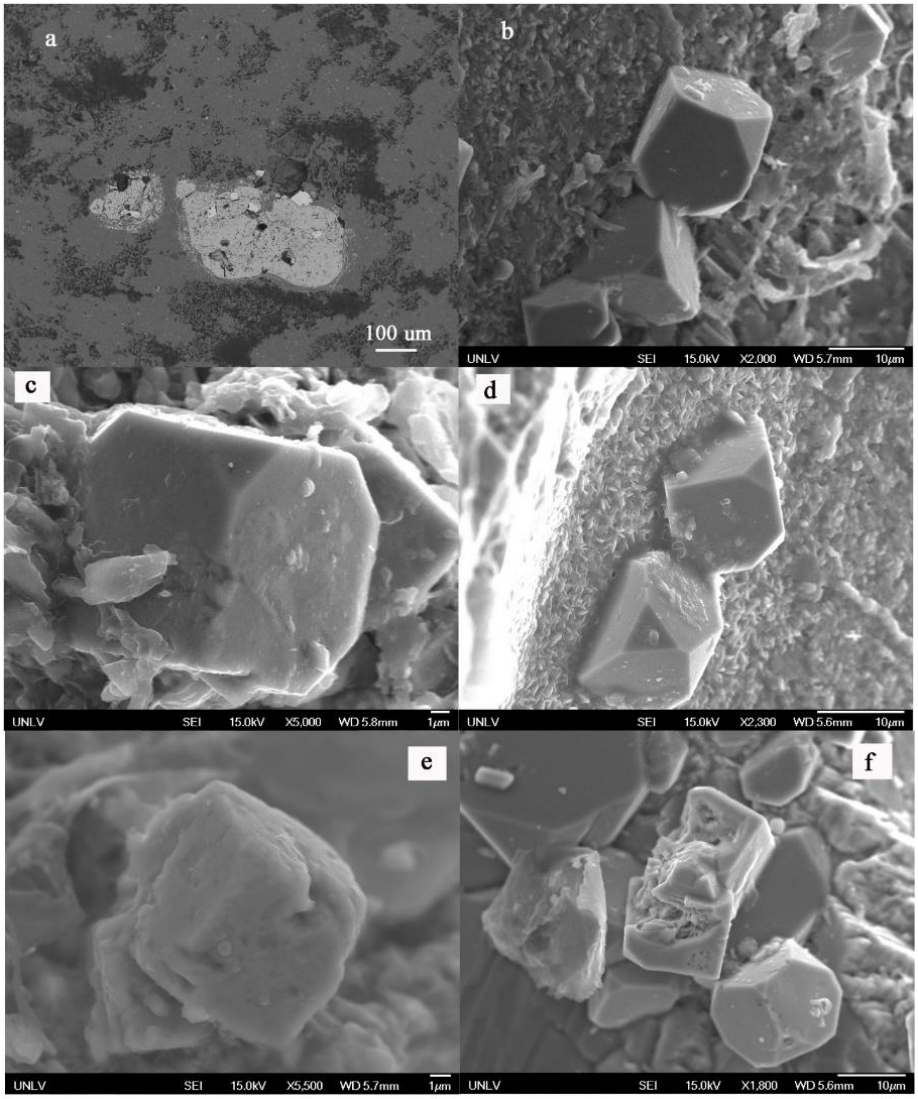


Figure 8. Images of greenalite and arsenogoyazite. (**a**) Subrounded grains of Si-Fe mineral (greenalite) coexists with magnetite (bright grains in the greenalite) in the matrix. (**b**–**d**) Arsenogoyazite crystals show their possible 3-fold axes, indicating a trigonal symmetry. (**e**,**f**) The dissolving pits on the arsenogoyazite crystals indicate their potential dissolving capability when touching meteoric water.

Within the vesicles, quartz, zircon, ilmenite, and alkali feldspar crystalize as euhedral phases. As–Sr–Al mineral exists in the vesicles.

4.2.6. As Minerals

As–Al–Sr minerals form as 10–20-micron euhedral crystals in the vesicles of the tuff (Figures 3b–d, 8b–f and 9) and Ar–Y phase has been found included in the biotite (Figure 4a). Their chemistry is reported in Table 4 and Supplementary Materials SI. The As–Al–Sr crystals show a cube shape. However, the crystal surface shape and distribution indicate that the crystal does not contain four-fold axes. The three-fold axes exist based on Figure 8b. Generally, only two-fold axes can be identified (Figure 8b–f) based on the BSE images of the crystals. The possible symmetry of this crystal might be trigonal. Electron microprobe data give the following results: SrO 4.6–13.1 wt.%, BaO 0–10 wt.%, CaO 0.2–1.8 wt.%, FeO 0.3–0.5 wt.%, Al_2O_3 28.6–35.9 wt.%, La_2O_3 1.6–6.6 wt.%, Ce_2O_3 0.9–8.4 wt.%, As_2O_5 32.4–35.2 wt.%, P_2O_5 1.0–5.3 wt.%, SO_3 0.1–1.9 wt.%. The chemistry of this mineral is similar to the reported arsenogoyazite, and the variable total indicates that the hydroxyl content in this phase might be variable in different mineral grains. This As phase contains more than 5 wt.% of REE oxides.

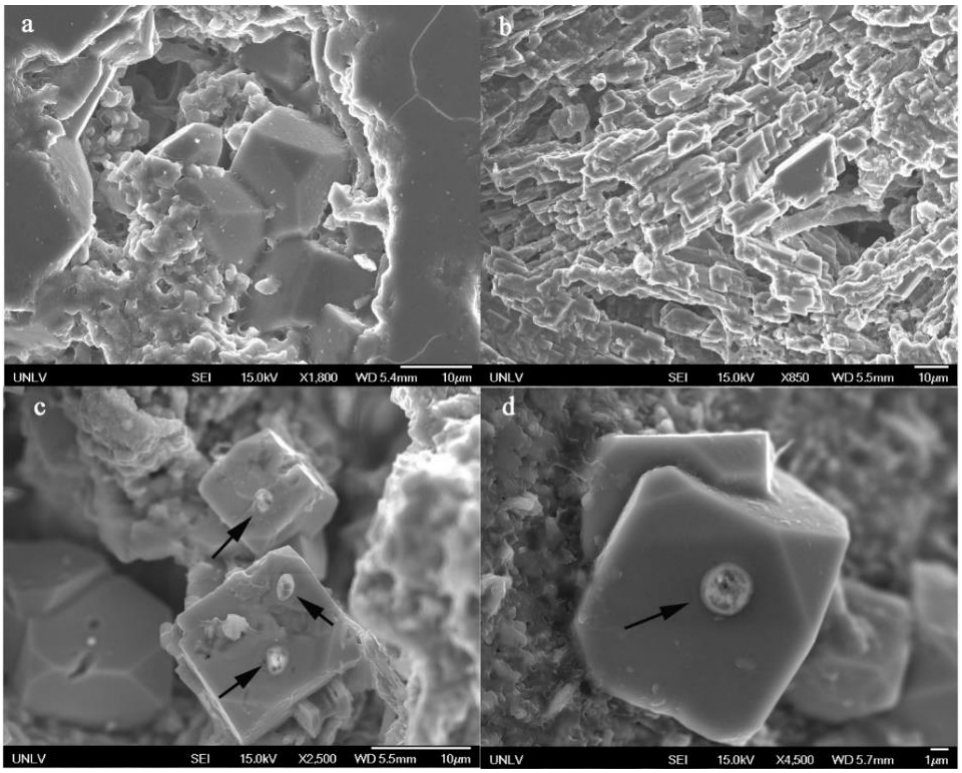


Figure 9. Images of crystals in the vesicles. (**a**) Euhedral quartz and sanidine in the cavity. (**b**) Subhedral sanidine aggregates. (**c**,**d**) Electron beam (15 kV/10 nA) damages the arsenogoyazite-like crystals (pointed by the arrow). The beam damage indicates the weak bounding feature of this crystal.

4.3. Whole-Rock Major and Trace Elements

Whole-rock major and trace elements from ICP-MS are listed in Table 5. Major elements are similar to the shard composition (Figure 5). The Chondrite-normalized REE and primitive mantle-normalized multi-element variations are plotted. The REE pattern shows a strong Eu anomaly and no clear enrichment in total REE (Figure 10a). The trace element pattern shows enrichment of K, a negative anomaly for Ta and Nb, and a strong negative anomaly of Ba, Sr, P, and Ti (Figure 10b).

Table 5. ICP-MS whole-rock major and trace elements.

	e93	e93-ot	e111	e115	e115-ot	2σ Uncert *
SiO_2 *	71.8	70.5	79.8	70.5	73.1	0.121
TiO_2	0.22	0.19	0.17	0.27	0.20	0.084
Al_2O_3	13.80	12.78	9.89	14.13	12.99	0.101
FeO	2.01	1.56	1.44	2.28	1.87	0.079
MnO	0.09	0.07	0.05	0.10	0.10	0.134
MgO	0.20	2.74	0.03	0.30	0.48	0.086
CaO	1.20	2.16	0.32	1.40	1.24	0.081
Na_2O	1.39	1.25	0.78	1.41	1.25	0.063
K_2O	9.08	8.34	6.60	9.29	8.36	0.077
P_2O_5	0.23	0.32	0.13	0.27	0.35	0.106
Total	100.01	99.90	99.21	99.96	99.94	
La	46.83	70.80	51.45	58.65	39.45	0.084
Ce	101.88	150.85	123.66	120.35	91.21	0.08
Pr	11.67	18.10	13.01	15.81	9.76	0.119
Nd	42.96	65.23	45.69	60.14	35.79	0.104
Sm	9.81	13.74	7.65	14.43	7.62	0.11
Eu	0.57	0.69	0.46	0.88	0.50	0.083
Gd	9.42	12.41	5.47	14.12	7.04	0.118
Tb	1.60	2.02	0.90	2.40	1.18	0.102
Dy	9.31	11.48	5.33	13.94	6.78	0.11
Ho	1.90	2.26	1.11	2.80	1.40	0.098
Er	5.26	6.32	3.24	7.58	3.93	0.135
Tm	0.80	0.96	0.53	1.16	0.61	0.173
Yb	5.01	5.85	3.36	6.95	3.85	0.136
Lu	0.71	0.84	0.50	0.97	0.56	0.076
Cr	2.48	3.23	1.54	3.11	2.93	0.113
Ni	3.88	2.08	1.61	9.74	2.92	0.103
Sc	3.85	4.77	3.04	3.78	3.64	0.087
V	4.41	6.27	5.26	6.62	5.37	0.068
Rb	396.62	402.97	285.97	364.58	359.31	0.049
Sr	424.57	645.66	75.00	552.21	347.35	0.069
Y	57.08	71.52	32.42	88.93	41.95	0.108
Zr	165.89	184.81	174.47	158.16	147.38	0.113
Nb	35.88	42.01	28.12	33.03	33.85	0.178
Ba	241.78	259.17	212.63	540.37	410.01	0.078
Hf	5.77	5.83	5.62	4.84	5.16	0.138
Ta	2.33	2.39	2.13	2.21	2.16	0.156
Pb	21.68	27.57	12.35	21.63	21.33	0.131
Th	19.83	21.31	18.84	18.21	18.09	0.122
U	3.15	3.48	2.67	3.31	3.16	0.103

* SiO_2 is from the average of the shard EPMA data. 2σ uncert—2σ uncertainty from BHVO.

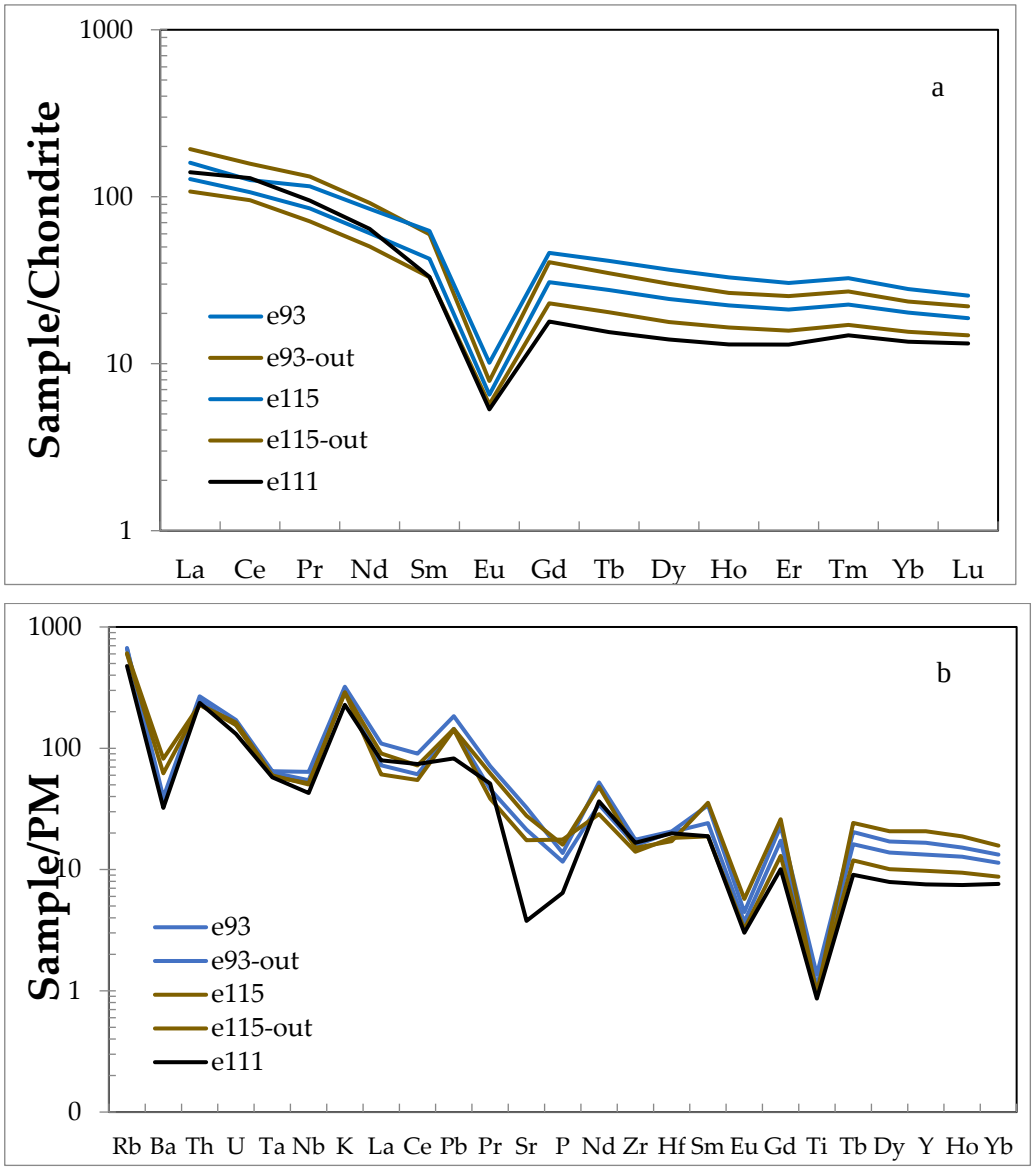


Figure 10. (**a**) REE chondrite normalized plot. (**b**) Trace elements primitive mantle-normalized plot.

5. Discussion

5.1. Arsenic Containing Minerals

Two types of arsenic-containing minerals are found in these rocks. One is the As–Al–Sr phase found in the vesicles of the tuff (Figures 3 and 8). The other is an As–Y phase as inclusions in mafic minerals (Figure 4a).

Based on the chemical character and the crystal shape, the As–Al–Sr phase quite possibly belongs to the arsenogoyazite $(Sr,Ca,Ba)Al_3(AsO_4,PO_4)_2(OH,F)_5 \bullet (H_2O)$ group, a trigonal mineral with As–Sr–Al components named in 1984 [25]. The three-fold axes can be observed in the crystal (Figure 8). The P and As contents are variable in each analysis (Table 4), which indicates a substitution between P and As. The studied As–Sr–Al phase contains 6 to 14 wt.% of REE. The high REE content in the studied As–Sr–Al phase makes it distinguished from the reported arsenogoyazite from the hydrothermal deposits in Europe [25]. The arsenoflorencite $(La,Sr)Al_3(AsO_4,SO_4,PO_4)_2(OH)_6$ is an REE-As mineral that has a similar crystal feature as arsenogoyazite. Because the studied As–Sr–Al phase is in the micron size range, its crystal structure is not worked in this study. We use the term "arsenogoyazite-like phase" when this mineral is mentioned in the rest of the paper.

The arsenogoyazite-like phase exists in all studied tuff samples; non-welded, partially welded, and densely welded tuffs. The partially welded tuff contains the most abundant of these crystals. They form clusters on the wall of the vesicles (Figures 3 and 8). After the eruption, the volatile component in the pyroclastic flow was concentrated during the diagenetic welding of volcanic tuff. Because of the high trace element content nature of these volcanic rocks, the arsenic and other trace elements (Sr and REE) formed the euhedral As–Sr–Al crystals in cavities. The euhedral alkali feldspars, quartz, zircon, and ilmenite co-exist with arsenogoyazite-like phase (Figure 4b–d, Figure 9a) and the vesicles sometimes contain micron-size prism shape feldspar (Figure 9b). Therefore, the arsenogoyazite-like crystals should be the vapor phase mineral crystallized in the lithogenesis stage of the pyroclastic flow.

The As–Y phase (a possible hydrated chernovite $YAsO_4$) exists as inclusions in the biotite. They might form in either of the following two conditions. (1) This As–Y phase could be the primary arsenic mineral formed in the early crystallization stage of the magma. They were included in the mafic minerals and brought up to the surface. During the formation of the tuff, volatile components carried in the pyroclastic flow can cause alteration of biotite and also change this As–Y phase into a hydrated mineral. (2) This As–Y mineral is a secondary phase formed along the cleavage or fracture in biotite. It might form in the tuff welding process as well. The compressing process caused the volatile components in the tuff to move along the fractures and mineral cleavages. Trace elements and volatile components might concentrate in the biotite fracture and form the As–Y mineral. In either case, the volcanic rock should be rich in arsenic and trace elements.

5.2. Whole-Rock Geochemistry

The aluminum saturation index (ASI) of shards shows that the rock is near the boundary of metaluminous to peralkaline. The rock has a high K/Na ratio, and K_2O is in the range of 6 to 11 wt.%. The REE and trace element patterns indicate a highly evolved magma. The trace element characteristics indicate that the rocks are enriched with K, Hf, Nb, Ta, and Y and depleted of Ba, Sr, P, and Ti (Table 5). The trace element pattern possesses the characteristics of the melt formed with the post-collisional and within plate environment (Figure 10). The negative Ba and Sr anomaly indicate that the magma itself contains low Ba and Sr. The Sr-rich and Ba-rich As phases should form in the late magmatic stage. The highly evolved volatiles joined the eruption process of the magmatism and crystalized the arsenogoyazite-like mineral in the vesicles as the vapor phases.

The Oligocene to Miocene silicic volcanic rocks is the largest igneous province in North America [23,26,27]. The hundreds of kilometers-wide volcanic eruptions extend for more than 2000 km. It is named as Sierra Madre Occidental unit, covering from the US–Mexico border to the Trans-Mexican Volcanic Belt. The crustal extension is suggested as one mechanism to generate large silicic magma volumes [28–30] and large magnitude explosive silicic eruptions [31]. This extension should correspond to the change in stress by the collision of the East Pacific Rise with North America, while a convergent margin (Farallon plate) changed to a transform margin along with the western North America plate [32]. The change is contemporaneous with a shift from subduction-related, continental volcanic arc magmatism to intraplate extensional magmatism.

Most of the rhyolites in the Sierra Madre Occidental belt erupted between 38 and 20 Ma [26,33,34]. The 38 to 20 Ma compositionally bimodal Sierra Madre Occidental igneous rocks are volumetrically dominant in the silicic component with SiO_2 68–75 wt.% [22,26,35,36]. Based on the similar eruption ages and physical characteristics of ignimbrite sequences described elsewhere in the region [23,37,38], silicic outflow ignimbrite sheets erupted at the studied area is the east volcanic units of the Sierra Madre Occidental, which mainly contains 28–30 Ma silicic volcanic rocks [39]. Therefore, the Sierra Madre Occidental ignimbrite flare-up might primarily be produced by crust melting, which was induced by the thermal energy from a massive generation of subcrustal mafic melts [17]. Felsic crust partial melting of the felsic crust needs a much less amount of primary mafic magmas

to produce rhyolite [40,41]. One portion of basalt may be produced from two-thirds to one equivalent volume of rhyolite on a one-hundred-year scale, while fraction crystallization of mafic magma generates a much less amount of rhyolite [41]. The high alkali rocks contain Fe-rich mafic phenocrysts and are named "ferroaugite rhyolite" [22]. The Acantilado tuff in the west and north of the city of Chihuahua has been classified as alkaline ignimbrite and contains fayalite and Na-Fe pyroxene [42]. Based on the stratigraphy of this area, the studied tuffs (samples e65 to e116) belong to this alkaline ignimbrite unit. There is no fayalite and aegirine found in these rocks, but the greenalite in sample e93 might be the altered phase of fayalite (Figure 8a). These rocks are possibly from calderas located to the west of the city of Chihuahua and the Ar ages from these tuffs give 29.98 to 30.17 Ma [11]. The peralkaline eruption should correlate with the regional extension environment.

The alkaline ignimbrite should generate from partial melting in the lower crust. The batholiths in the upper crust in the region probably represent the significant proportion of Mesozoic to Early Tertiary age igneous intrusions that may have resided in the lower crust immediately before the ignimbrite "flare-up". The regional basement rocks and crustal structure beneath the Cenozoic volcanic tuff include lower volcanic complex containing crustal batholiths, arc-backarc volcanic-sedimentary rocks, metasedimentary rocks, and gneissic basement [39,43,44]. This basement is interpreted as a continental-slope deposit, which is made up of a thick succession of Paleozoic deep-marine turbidites that override on the shelf rocks [45,46]. The different chemical characters in the feldspar composition (Figure 6) from different Cenozoic volcanic tuffs may reflect that the eruptions might generate from different magma sources or eruptions from different evolution stages of the magma chamber. The Ba content in sanidine usually corresponds to the P-T condition of the melt [47]. In the studied samples, the sanidine in the matrix is crystallized from the melt in the eruption stage; the moderate amount of Ba (0.5–1 wt.%, Table 2) and An content (2–3 An) in the matrix sanidine indicate a high temperature, low pressure, and volatile-rich condition. The ignimbrite eruptions should correlate with the recharging of highly evolved flux into the magma chamber. The recharging material contains enriched volatile and incompatible elements. More whole-rock geochemical work is needed to evaluate the magmatism in this region.

5.3. Possible REE Source

The mineral chemistry indicates that this Tertiary volcanic rock is rich in Ba, Sr, As, and REE. Both biotite and feldspar contain high BaO (Figures 6 and 7), and the crystallization of arsenogoyazite-like phase indicates the high As, Sr, and REE feature of the Tertiary alkaline volcanic rocks. The long temporal evolution of the Tertiary magmatism in the extensional environment might concentrate the incompatible trace elements in the vapor phase of this type of volcanic rock.

The crustal component might be the supplier of the As, Sr, Ba, and REE in the alkaline tuff. Shale could be a major supply of arsenic. USGS standard black shale (SDO-1) has an As content of 68.5 ppm [48]. Based on a worldwide dataset, shales can have a mean As content of about 15 ppm, and carbonaceous black shales can contain a mean As of 29 ppm, compared to normal crustal rocks, which contain 1 to 4 ppm [49,50]. Ketris and Yudovitch [51] reported a background mean of 30 ppm As, with a strongly anomalous range of 130 to 180 ppm As, from over 4000 black shale analyses. In contrast, mean arsenic values for igneous rocks are 0.7 ppm for basalt and gabbro and 3 ppm As for granite and granodiorite [52]. A geochemistry comprehensive study of granites has revealed that the crust source S-type granites have an average of 9 ppm As, while the igneous source I-type granites have an average of 5 ppm As [53]. Therefore, the crustal partial melting and assimilation of the continental-slope basement might be the source for As in the Cenozoic volcanic tuff.

Deep crustal melting can cause the marked enrichment of Ba and Sr during subduction. The geochemical characters of the Sierra Madre Occidental rhyolites, which show spatial variations in trace elements (e.g., high field strength element (HFSE) and large-ion lithophile

elements (LILE)), are correlated with the composition of the basement rocks [54]. The volcanic rocks in other volcanic arcs also indicate the basement rock influence on the trace element characters [54,55]. Crustal components clearly contribute more to the K, Ba, and Light Rare Earth Elements (LREE) for the melt, which is indicated by the following observations. Along with the increase in crust thickness, there are rises of K_2O, Ba, Ce, and declines of FeO*/MgO in the late Quaternary volcanic systems in the Andes of Central Chile [55]. The marine sedimentary deposit may supply the high Ba, Sr, and As components to the volcanic system [55]. The crustal melts and fluids along with the hot columns beneath long-lived centers contribute Ba-Sr way more than the slab-derived component [28]. The experimental studies also demonstrate that a low portion of partial melting of basaltic rocks could produce the high Ba–Sr contents in acidic magma at P–T conditions of 1000–1100 °C and 8–32 kPa [56]. The studies of the chemical zoning of Bishop Tuff and Bandelier Tuff indicate that the less fractionated magma recharge could generate high Ti, Sr, and Ba rhyolite [57]. The Sierra del Cuervo tuffs should be equivalent to the 30 Ma Acantilado tuff, which is exposed at the north and west of the city of Chihuahua [25,40]. These alkaline tuffs are on top of the regional calcalkaline suites and should be generated by partial melting during the extensional tectonic regime. The mineralogical and geochemical aspects indicate the post-tectonic nature of these Tertiary volcanic rocks (Figure 10). The extensional-induced partial dehydration melting formed these alkaline melts in the lower crustal blocks. Low Ca, high FeO/MgO, K-rich alkaline, high contents of Rb, Sr, Ba, Y, and LREE characteristics point to the extensional crustal melting features of these late-stage Tertiary rocks in the region. The high Ba-Sr felsic magmatism was most probably the result of partial delamination or convective activity during the rollback of the subducting Pacific Plate. The recharging of the alkaline melt into the Cenozoic volcanic magma chamber might contribute to the K, Ba, Sr, LREE, and As in the vapor phase crystallization.

5.4. As in Groundwater

Based on all data collected, the Tertiary volcanic tuffs are the main source for the high arsenic content in the local groundwater. Geological characteristics of rocks and sediments can influence groundwater chemistry [58], and different water–rock interaction models have been used to evaluate the pollution processes [59–61]. Because the current work does not include any dissolving test for those arsenic minerals and the tuffs, it is not possible to build a dissolution model for the Sierra del Cuervo volcanic tuffs. However, based on the surface features of the arsenogoyazite-like phases, it shows that some crystal surfaces have been dissolved (Figure 8e,f). The arsenogoyazite-like crystal is also sensitive to the electron beam and can be damaged by the electron beam, which is a characteristic of hydrated minerals under the electron beam. During the electron microprobe analysis, the electron beam generates a burning mark on the crystal surface (Figure 9c,d). The beam damage on the crystals usually happens on the volatile-containing minerals. EPMA analyses on hydrated minerals result in cratering due to heating within the electron interaction volume. The low total of the EPMA analysis for the As–Sr–Al phase also indicates the existence of hydroxyl/water in this phase. There is no solubility information of the arsenogoyazite itself. Based on the webmineral.com/data/Arsenogoyazite from the Mineralogy database, the arsenogoyazite $(Sr,Ca,Ba)Al_3(AsO_4,PO_4)_2(OH,F)_5 \bullet (H_2O)$ is a hydrated mineral. Therefore, these arsenogoyazite-like phases should be soluble in the water. The arid weather condition of the Chihuahua desert preserves these crystals in the volcanic tuff. The occasional rainfall can partially dissolve the As–Sr–Al mineral and bring the arsenic into the groundwater.

6. Conclusions

Arsenogoyazite-like arsenic minerals have been identified in Cenozoic volcanic tuff at Tabalaopa Basin, city of Chihuahua, Mexico. The Tabalaopa Basin contains volcanic strata and the unconsolidated Quaternary deposit. Cenozoic volcanic tuff forms a low hill terrene in this area. The exposed reddish color volcanic rocks are felsic welded tuff and rhyolite. Sanidine, quartz, and biotite phenocrysts show linear distribution within

the fine grain matrix. The rocks contain a large number of vesicles that are foliated with the welding bends. White, honey-color and colorless micron-sizes crystals grow on the wall of the cavities, and the majority of them are K-feldspar, quartz, Ti-Fe oxide, and a few zircons. The arsenic-containing crystals are coexisting with those euhedral minerals. The arsenogoyazite-like crystals in the cavities are dozens of micrometers in size. The arsenic minerals formed in the vapor stage during the formation of the volcanic tuff. The relative soluble characteristics of the arsenogoyazite-like phase make this mineral to be leached by meteoric water. The precipitation can deliver arsenic in the groundwater. Because of the high LREE contents in the arsenogoyazite-like minerals and their soluble characteristics, it is worth reevaluating the REE content in the Tertiary alkaline volcanic rocks in this region as well.

Supplementary Materials: The following supporting information can be downloaded at: https://www.mdpi.com/article/10.3390/geosciences12020069/s1, SI: EPMA data in Excel file; SII: Location of wells and images of volcanic rock outcrops.

Author Contributions: The conceptualization of this work is from J.A.R.-P. and M.R. Field sampling is from J.A.R.-P. and P.G. Petrographic work is from M.R. and P.G. Mineral characterization and chemistry are from M.R. All authors have read and agreed to the published version of the manuscript.

Funding: This research received no external funding.

Data Availability Statement: All data in this manuscript are from the work of the authors. A full set of mineral chemical data and the field information are reported in the supplementary files.

Acknowledgments: We thank the UTEP microprobe lab, which provided the full section X-ray maps and a portion of mineral chemical data. We thank EMiL and LVIS labs for FESEM, EPMA, and ICP-MS analyses. We thank the editorial work from assistant editors and the suggestive comments from reviewers.

Conflicts of Interest: The authors declare no conflict of interest.

References

1. Welch, A.H.; Westjohn, D.B.; Helsel, D.R.; Wanty, R.B. Arsenic in groundwater of the United States: Occurrence and geochemistry. *Groundwater* **2000**, *38*, 589–604. [CrossRef]
2. González-Horta, C.; Ballinas-Casarrubias, L.; Sánchez-Ramírez, B.; Ishida, M.C.; Barrera-Hernández, A.; Gutiérrez-Torres, D.; Zacarias, O.L.; Saunders, R.J.; Drobna, Z.; Mendez, M.A.; et al. A Concurrent Exposure to Arsenic and Fluoride from Drinking Water in Chihuahua, Mexico. *Int. J. Environ. Res. Public Health* **2015**, *12*, 4587–4601. [CrossRef]
3. Smedley, P.L.; Kinniburgh, D.G. A review of the source, behaviour and distribution of arsenic in natural waters. *Appl. Geochem.* **2002**, *17*, 517–568. [CrossRef]
4. Fuoco, I.; De Rosa, R.; Barca, D.; Figoli, A.; Gabriele, B.; Apollaro, C. Arsenic polluted waters: Application of geochemical modelling as a tool to understand the release and fate of the pollutant in crystalline aquifers. *J. Environ. Manag.* **2022**, *301*, 113796. [CrossRef]
5. Rodrıgueza, R.; Ramos, J.A.; Armienta, A. Groundwater arsenic variations: The role of local geology and rainfall. *Appl. Geochem.* **2004**, *19*, 245–250. [CrossRef]
6. Abdullah, M.I.; Shiyu, Z.; Mosgren, K. Arsenic and selenium species in the oxic and anoxic waters of the Oslofjord, Norway. *Mar. Pollut. Bull.* **1995**, *31*, 116–126. [CrossRef]
7. Rodriguez-Pineda, J.A. A Geophysical, Geochemical and Remote Sensing Investigation of the Water Resources at the City of Chihuahua, Mexico. Ph.D. Thesis, Department of Geology, University of Texas, El Paso, TX, USA, 2000.
8. Mahlknecht, J.; Horst, A.; Hernandez-Limon, G.; Aravena, R. Groundwater geochemistry of the Chihuahua City region in the Rio Conchos Basin (northern Mexico) and implications for water resources management. *Hydrol. Processes* **2008**, *22*, 4736–4751. [CrossRef]
9. Comité de la Carta Geológica de México; Universidad Nacional Autónoma de México; Instituto de Geología. *Carta Geológica de la República Mexicana, Escala 1:2000000*; Universidad Nacional Autónoma de México and Instituto de Geología: Mexico City, Mexico, 1962.
10. Handschy, J.W.; Dyer, R. Polyphase deformation in Sierra del Cuervo, Chihuahua, Mexico: Evidence for Ancestral Rocky Mountain tectonics in the Ouachita foreland of northern Mexico. *Geol. Soc. Am. Bull.* **1987**, *99*, 618–632. [CrossRef]
11. McDowell, F.W.; McIntosh, W.C. Timing of intense magmatic episodes in the northern and central Sierra Madre Occidental, western Mexico. *Geosphere* **2012**, *8*, 1505–1526. [CrossRef]
12. Flawn, P.T.; Goldstein, A., Jr.; King, P.B.; Weaver, C.E. *The Ouachita System*; Bureau of Economic Geology, University of Texas Publication: Austin, TX, USA, 1961.

13. Stege, B.R. Stratigraphy and Significance of the Carbonates of the Peña Blanci Uranium District, Chihuahua, Mexico. Master's Thesis, University of Texas, El Paso, TX, USA, 1979; 81p.
14. Gries, J.C. Problems of delineation of the Rio Grande Rift into the Chihuahua tectonic belt of northern Mexico. In *Rio Grande Rift: Tectonics and Magmatism*; Riecker, R.E., Ed.; AGU: Washington, DC, USA, 1979; Volume 14, pp. 107–113.
15. Hennings, P.H. Structural transect of the southern Chihuahua Fold Belt between Ojinaga and A'dama, Chihuahua, Mexico. *Tectonics* **1994**, *13*, 1445–1460. [CrossRef]
16. Humphreys, E.D. Post-Laramide removal of the Farallon slab, western United States. *Geology* **1995**, *23*, 987–990. [CrossRef]
17. Ferrari, L.; López-Martinez, M.; Rosas-Elguera, J. Ignimbrite flare-up and deformation in the southern Sierra Madre Occidental, western Mexico—Implications for the late subduction history of the Farallon plate. *Tectonics* **2002**, *21*, 17-1–17-24. [CrossRef]
18. Murray, B.P.; Busby, C.J.; Ferrari, L.; Solari, L.A. Synvolcanic crustal extension during the mid-Cenozoic ignimbrite flare-up in the northern Sierra Madre Occidental, Mexico: Evidence from the Guazapares Mining District region, western Chihuahua. *Geosphere* **2013**, *9*, 1201–1235. [CrossRef]
19. McDowell, F.W. Geologic Transect across the Northern Sierra Madre Occidental Volcanic Field, Chihuahua and Sonora, Mexico. *Geol. Soc. Am.* **2007**, *6*, 70p.
20. Campbell, A.R. Volcanic Rocks of the La Perla Area, Chihuahua, Mexico. Master's Thesis, University of Texas, Austin, TX, USA, 1977; 110p.
21. Keller, P.C.; Bockover, N.T.; McDowell, F.W. Tertiary volcanic history of the Sierra del Gallego area, Chihuahua, Mexico. *Geol. Soc. Am. Bull.* **1982**, *93*, 303–314. [CrossRef]
22. Cameron, M.; Bagby, W.C.; Cameron, K.L. Petrogenesis of voluminous mid-tertiary ignimbrites of the Sierra Madre Occidental. *Contrib. Mineral. Petrol.* **1980**, *74*, 271–284. [CrossRef]
23. Cather, S.M.; Dunbar, N.W.; McDowell, F.W.; McIntosh, W.C.; Scholle, P.A. Climate forcing by iron fertilization from repeated ignimbrite eruptions: The icehouse-silicic large igneous province (SLIP) hypothesis. *Geosphere* **2009**, *5*, 315–324. [CrossRef]
24. Bryan, S.E.; Ferrari, L.; Reiners, P.W.; Allen, C.M.; Petrone, C.M.; Ramos-Rosique, A.; Campbell, I.H. New Insights into Crustal Contributions to Large-volume Rhyolite Generation in the Mid-Tertiary Sierra Madre Occidental Province, Mexico, Revealed by U-Pb Geochronology. *J. Petrol.* **2008**, *49*, 47–77. [CrossRef]
25. Walenta, K.; Dunn, P.J. Arsenogoyazit, ein neues Mineral der Crandallitgruppe aus dem Schwarzwald. *Schweiz. Mineral. Und Petrogr. Mitt.* **1984**, *64*, 11–19. (In German)
26. McDowell, F.W.; Clabaugh, S.E. Ignimbrites of the Sierra Madre Occidental and their relation to the tectonic history of western Mexico. In *Ash-Flow Tuffs*; Chapin, C.E., Elston, W.E., Eds.; Geological Society of America: Boulder, CO, USA, 1979; Volume 180, pp. 113–124.
27. Ferrari, L.; Valencia-Moreno, M.; Bryan, S. Magmatism and tectonics of the Sierra Madre Occidental and its relation with the evolution of the western margin of North America. In *Geology of Mexico: Celebrating the Centenary of the Geological Society of Mexico*; Alaniz-Àlvarez, S.A., Nieto Samaniego, A.F., Eds.; Geological Society of America: Boulder, CO, USA, 2007; Volume 422, pp. 1–39.
28. Hildreth, W. Gradients in silicic magma chambers: Implications for lithospheric magmatism. *J. Geophys. Res.* **1981**, *86*, 10153–10192. [CrossRef]
29. Wark, D.A. Oligocene ash flow volcanism, northern Sierra Madre Occidental: Role of mafic and intermediate-composition magmas in rhyolite genesis. *J. Geophys. Res.* **1991**, *96*, 13389–13411. [CrossRef]
30. Hanson, R.B.; Glazner, A.F. Thermal requirements for extensional emplacement of granitoids. *Geology* **1995**, *23*, 213–216. [CrossRef]
31. Costa, A.; Gottsmann, J.; Melnik, O.; Sparks, R.S.J. A stress-controlled mechanism for the intensity of very large magnitude explosive eruptions. *Earth Planet. Sci. Lett.* **2011**, *310*, 161–166. [CrossRef]
32. Henry, C.D.; Price, J.G.; James, E.W. Mid-Cenozoic stress evolution and magmatism in the southern Cordillera, Texas and Mexico: Transition from continental arc to intraplate extension. *J. Geophys. Res.* **1991**, *96*, 13545–13560. [CrossRef]
33. McDowell, F.; Keizer, R.P. Timing of mid-Tertiary volcanism in the Sierra Madre Occidental between Durango city and Mazatlán, Mexico. *Geol. Soc. Am. Bull.* **1977**, *88*, 1479–1487. [CrossRef]
34. McDowell, F.W.; Mauger, R.L. K-Ar and U-Pb zircon chronology of Late Cretaceous and Tertiary magmatism in central Chihuahua State, Mexico. *Geol. Soc. Am. Bull.* **1994**, *106*, 118–132. [CrossRef]
35. McDowell, F.W.; Roldan-Quintana, J.; Connelly, J. Duration of Late Cretaceous-early Tertiary magmatism in east-central Sonora, Mexico. *Geol. Soc. Am. Bull.* **2001**, *113*, 521–531. [CrossRef]
36. Bryan, S.E. Silicic Large Igneous Provinces. *Episodes* **2007**, *30*, 20–31. [CrossRef]
37. Swanson, E.R.; Kempter, K.A.; McDowell, F.W.; McIntosh, W.C. Major ignimbrites and volcanic centers of the Copper Canyon area; a view into the core of Mexico's Sierra Madre Occidental. *Geosphere* **2006**, *2*, 125–141. [CrossRef]
38. Verma, S.; Carrasco-Núñez, G. Reappraisal of the Geology and Geochemistry of Volcán Zamorano, Central Mexico: Implications for Discriminating the Sierra Madre Occidental and Mexican Volcanic Belt Provinces. *Int. Geol. Rev.* **2003**, *45*, 724–752. [CrossRef]
39. Orozco-Esquivel, M.T.; Nieto-Samaniego, A.F.; Alaniz-Álvarez, S. Origin of rhyolitic lavas in the Mesa central, Mexico, by crustal melting related to extension. *J. Volca. Geoth. Res.* **2002**, *118*, 37–56. [CrossRef]
40. Huppert, H.E.; Sparks, R.S.J. The generation of granitic magmas by intrusion of basalt into continental crust. *J. Petrol.* **1988**, *29*, 599–642. [CrossRef]
41. Harry, D.L.; Leeman, W.P. Partial melting of melt metasomatized subcontinental mantle and the magma source potential of the lower lithosphere. *J. Geophys. Res.* **1995**, *100*, 10255–10269. [CrossRef]

42. Mauger, R.L. The mid-Eocene Majalca Canyon caldera, Chihuahua, Mexico. In *Geology and Mineral Resources of Northern Sierra Madre Occidental, Mexico: Guidebook for the 1992 Field Conference*; Clark, K.F., Roldán- Quintana, J., Schmitt, R.H., Eds.; El Paso Geological Society: El Paso, TX, USA, 1992; pp. 127–132.
43. Centeno-García, E.; Guerrero-Suastegui, M.; Talavera-Mendoza, O. The Guerrero Composite Terrane of western Mexico: Collision and subsequent rifting in a supra-subduction zone. In *Formation and Applications of the Sedimentary Record in Arc Collision Zones*; Draut, A., Clift, P.D., Scholl, D.W., Eds.; Geological Society of America: Boulder, CO, USA, 2008; Volume 436, pp. 279–308.
44. Draut, A.E.; Clift, P.D.; Scholl, D.W.; Ryan, P.D.; Waltham, D.; Hall, R.; Smyth, H.R.; Ebinger, C.J.; Dorobek, S.L.; Hoffmann, G.; et al. *Formation and Applications of the Sedimentary Record in Arc Collision Zones; Geological Society of America: Boulder, CO, USA, 2008; 435p.*
45. Coney, P.J.; Campa, M.F. *Lithotectonic Terrane Map of México (West of the 91st Meridian)*; Reston, Va.: Denver, CO, USA, 1987.
46. Stewart, J.H.; Roldán-Quintana, J. Upper Triassic Barranca Group: Nonmarine and shallow-marine rift-basin deposits of northwestern Mexico. In *Studies of Sonoran Geology*; Pérez-Segura, E., Jacques Ayala, C., Eds.; Geological Society of America: Boulder, CO, USA, 1991; Volume 254, pp. 19–36.
47. Gao, J.; Green, T.H. Barium partitioning between alkali feldspar and silicate liquid at high temperature and pressure. *Contrib. Miner. Pet.* **1989**, *102*, 328–335. [CrossRef]
48. Meyers, P.A.; Pratt, L.M.; Nagy, B. Introduction to geochemistry of metalliferous black shales. *Chem. Geol.* **1992**, *99*, 7–11. [CrossRef]
49. Boyle, R.W.; Jonasson, I.R. The geochemistry of arsenic and its use as an indicator element in geochemical prospecting. *J. Geochem. Explor.* **1973**, *2*, 251–296. [CrossRef]
50. Quinby-Hunt, M.S.; Wide, P.; Berry, W.B.N. Element geochemistry of low calcic black shales—statistical comparison with other shales. *U.S. Geol. Surv. Circ.* **1989**, *1037*, 8–15.
51. Ketris, M.P.; Yudovitch, Y.E. Estimations of Clarkes for Carbonaceous biolithes: World averages for trace element contents in black shales and coals. *Int. J. Coal Geol.* **2009**, *78*, 135–148. [CrossRef]
52. Reimann, C.; de Caritat, P. *Chemical Elements in the Environment: Fact Sheets for the Geochemist and Environmental Scientist*; Springer: Berlin, Germany, 1998; 398p.
53. Chappell, B.W. A chemical database for the New England batholith. In Proceedings of the New England Orogen Conference, University of New England, Armidale, NSW, Australia; 2010; pp. 119–123.
54. Albrecht, A.; Goldstein, S.L. Effects of basement composition and age on silicic magmas across an accreted terrane-Precambrian crust boundary, Sierra Madre Occidental, Mexico. *J. S. Am. Earth Sci.* **2000**, *13*, 255–273. [CrossRef]
55. Hildreth, W.; Moorbath, S. Crustal contributions to arc magmatism in the Andes of Central Chile. *Contrib. Miner. Pet.* **1988**, *98*, 455–489. [CrossRef]
56. Rapp, R.P.; Watson, E.B. Dehydration melting of metabasalt at 8-32 kbar: Implications for continental growth and crust-mantle recycling. *J. Petrol.* **1995**, *36*, 891–931. [CrossRef]
57. Hervig, R.L.; Dunbar, N.W. Cause of chemical zoning in the Bishop (California) and Bandelier (New Mexico) magma chambers. *Earth Planet. Sci. Lett.* **1992**, *111*, 97–108. [CrossRef]
58. Reyes-Gómez, V.M.; Alarcón-Herrera, M.T.; Gutiérrez, M.; López, D.N. Fluoride and Arsenic in an Alluvial Aquifer System in Chihuahua, Mexico: Contaminant Levels, Potential Sources, and Co-occurrence. *Water Air Soil Pollut.* **2013**, *224*, 1433. [CrossRef]
59. Morán-Ramírez, J.; Ledesma-Ruiz, R.; Mahlknecht, J.; Ramos-Leal, J.A. Rockewater interactions and pollution processes in the volcanic aquifer system of Guadalajara, Mexico, using inverse geochemical modeling. *Appl. Geochem.* **2016**, *68*, 79–94. [CrossRef]
60. Apollaro, C.; Fuoco, I.; Bloise, L.; Calabrese, E.; Marini, L.; Vespasiano, G.; Muto, F. Geochemical Modeling of Water-Rock Interaction Processes in the Pollino National Park. *Geofluids* **2021**, *2021*, 6655711. [CrossRef]
61. Apollaro, C.; Di Curzio, D.; Fuoco, I.; Buccianti, A.; Dinelli, E.; Vespasiano, G.; Castrignanò, A.; Rusi, S.; Barca, D.; Figoli, A.; et al. A multivariate non-parametric approach for estimating probability of exceeding the local natural background level of arsenic in the aquifers of Calabria region (Southern Italy). *Sci. Total Environ.* **2022**, *806*, 150345. [CrossRef] [PubMed]